Detwinning Phenomenon and Its Effect on Resulting Twinning Structure of an Austenitic Hadfield Steel

MARINA LUKAS, GERALD RESSEL, CAROLA HAHN, SVEN ECK, BERNHARD SARTORY, THOMAS TITZE, and UWE OSSBERGER

Hadfield Steel shows high strain hardening which can be linked to its ability to form twins during mechanical loading. Twinning in Hadfield Steel is well documented, however, detwinning in Hadfield Steel is only barely investigated. Detwinning provides an additional contribution to plastic deformation, therefore it might be an essential effect during cyclic loading. In order to gain more information regarding the deformation behavior in Hadfield Steel, the present work concentrates on the twinning and detwinning behavior during interrupted tensile tests. Tensile tests were conducted in situ within a scanning electron microscope and interrupted at predefined elongations. To determine the formation of twins during every interruption, the electropolished tensile test sample was analyzed by electron backscatter diffraction. The first twins appeared after 5 to 10 pct strain. Conversely, tensile test interruptions at 30 and 40 pct elongation showed partial detwinning of the twinned regions. Furthermore, the Kernel Average Misorientation of the twinned and detwinned regions was analyzed. High values of misorientation were found not only in the twinned but also in the detwinned regions, thus the high level of misorientation can be linked to the twinning/detwinning process.

I. FUNDAMENTALS

A. *Hadfield Steel*

HADFIELD Steel was developed in 1882 by Sir Robert Hadfield[1] and combines an initially low yield strength (YS) of 200 to 400 MPa[2–6] with an exceptional ability to work harden (ultimate tensile strength (UTS) 800 to 1000 MPa[2,7,8]) and a high ductility with elongations at fracture of 50 to 80 pct.[9] The strong work hardening ability of the austenitic Hadfield Steel is ascribed to the dynamic Hall–Petch-Effect, where the microstructure is continuously refined by twinning during deformation.[10–12] Similar to grain boundaries, twin boundaries represent obstacles against dislocation movement which results in strengthening.[13] This effect of high strain hardening is also used in twinning induced plasticity (TWIP) steels. The ability to form twins in face centered cubic (fcc) austenitic steels upon deformation is determined by the stacking fault energy (SFE), with must be in the range between ~ 20 and 40 mJ/m^2 for twinning.[14] Hadfield Steel has a chemical composition of 1.05 to 1.35 wt pct C and a minimum of 11.0 wt pct Mn[15] and its stacking fault energy value has been reported between ~20 to 50 mJ/m^2 by different authors.[8,16–22]

B. *Deformation Twinning*

In an austenitic fcc microstructure, the {111}-plane is slip-plane and also twinning-plane, but the slip- and in most frequently present twin-direction are different and are <110> and <112>, respectively.[14] From the point of crystallography the most frequently present twin structure is a Σ3 twin, which is characterized by a 60 deg rotation around a <111>-axis.[23] The critical resolved shear stress (CRSS), which is needed for deformation twin formation (called critical twinning stress) is higher than for the slip of dislocations[24,25] and the nucleation of deformation twins requires also precedent dislocation activity.[26,27] A single deformation twin has a thickness of about 10 to 40 nm. However, upon further straining further twins form and may also align in bundles with the same orientation. These twin bundles have thicknesses above 100 nm and are thus also detectable by electron backscatter diffraction (EBSD).[14,28,29]

MARINA LUKAS, GERALD RESSEL, CAROLA HAHN, SVEN ECK and BERNHARD SARTORY are with the Materials Center Leoben Forschung GmbH, Leoben, 8700, Austria. Contact e-mail: marina.lukas@mcl.at THOMAS TITZE and UWE OSSBERGER are with the Voestalpine Railway Systems GmbH, Zeltweg, 8740, Austria.

C. Detwinning Mechanism

The annihilation or reversal of deformation twinning due to changed loading conditions is called detwinning. Detwinning has been reported for hexagonal Mg alloys, where twinning and detwinning is much easier than for fcc structures,[30–32] but also some studies on detwinning in fcc materials exist. Wang et al.[33] analyzed detwinning in Cu for nanoscale twins with HRTEM during straining. It was observed that detwinning happens when an extended dislocation redissociates during passing through a twin boundary. Ni et al.[34] also found detwinning of nano twins for a nickel alloy subjected to high pressure torsion (HPT) by the interaction of Shockley partials with the twin boundary. For nano-sized twins, Cao et al.[35] determined detwinning via secondary twinning after HPT in fcc duplex stainless steel. Another examination of the detwinning process in fcc materials was reported by Szczerba et al.[36,37] The publications give evidence for the existence of three different detwinning modes. Due to symmetry reasons, an atom on a {111}-plane in a fcc twin can move along three different <112> directions to restore the matrix fcc lattice.[36] However, only one of these movements is able to restore the original matrix orientation and the dislocation arrangement (called reverse twinning), whereas the two other detwinning modes only restore the matrix orientation, but not the dislocation arrangement (called pseudo-reverse twinning). During the pseudo-reverse twinning, most of the dislocations in the twinned region are transferred into a sessile configuration leading to strain hardening[36] and the CRSS for pseudo-reverse twinning is two times higher than for reverse twinning and about four times higher than for deformation twinning.[37] In the polycrystalline Fe-24Mn-3Al-2Si-1Ni-0.06C TWIP steel, McCormack et al.[14] found experimental evidence for detwinning during interrupted tension to compression loading. Localized shear is introduced into a grain upon deformation twinning, which leads to the formation of back-stresses in the surrounding matrix. Upon load reversal, these back-stresses enable detwinning.[14] Detwinning of high Mn TWIP steels was also extensively analyzed by D'Hondt et al.[38] by atomic force microscopy and digital image correlation. Mohammadzadeh et al. conducted a molecular dynamic simulation study on the atomic structure of a fcc Fe-22Mn nanocrystalline TWIP steel for tension to compression loading.[39] The simulation results showed annihilation of deformation twins and stacking faults and thus support the results found by McCormack et al.[14]

In comparison to deformation twinning, which is extensively studied for fcc materials,[26,28,29,40–43] detwinning has received much less attention. Thus, the present work focuses on the observation of twinning and detwinning in a the fcc Hadfield Steel during interrupted in situ tensile tests, which comprised repeated tensile loading and unloading sequences. The twinning and detwinning process was analyzed during the interruptions with scanning electron microscopy (SEM) and EBSD. The coupling of these characterization methods, i.e. tensile tests and EBSD measurements, gives the possibility to trace the crystallographic behavior of distinct positions subjected to tensile loading and unloading. The results show that partial detwinning of the twinned regions occurs during a few tensile loading/unloading cycles and that the twinning and detwinning process affects the locally present misorientation determined by EBSD. Furthermore, conventional tensile tests were conducted and the macroscopic twinning stress determined by the stress to strain curve was compared with the EBSD results.

II. EXPERIMENTAL

The Hadfield Steel used for the investigations had a chemical composition of 11.9 wt pct Mn, 1.05 wt pct C, Fe balance. The heat treatment of the Hadfield Steel comprised holding at 1050 °C for 15 minutes followed by water quenching.

For evaluation of the macroscopic twinning stress and the yield stress, a conventional tensile test was carried out according to the standard DIN EN 6892-1 on a Zwick BS1-FR250SN.A4.010 testing machine. A round tensile test specimen with 5 mm diameter and 25 mm gauge length was used (geometry based on DIN 50125-2009-07).

The in situ tensile test coupled with EBSD analysis was conducted using a flat tensile test specimen with an original width of 5 mm, a thickness of 1.5 mm and a gauge length of 20 mm. The specimen was electropolished from both sides on a Struers LectroPol-5 with Struers A2 electrolyte at + 5 °C start temperature and a voltage between 30 and 37 V. To protect the already polished side, a masking lacquer (Schlötter masking lacquer ochre No. 642000) was applied and removed later on by acetone. As electropolishing does not remove material evenly across the gauge length, the specimen varied in thickness and an exact determination of the stress and strain values was not possible. Therefore, the sample thickness due to electropolishing is estimated to be reduced to approx. 1 mm. The in situ tensile test was interrupted at different predefined elongations, in order to allow SEM and EBSD measurements at different elongations. Loading was conducted with a rate of 5 μm on a 15 kN loading stage (MZ.Mb-L-180226-BK, KammrathWeiss GmbH) and the loading direction in the SEM/EBSD images was parallel to the x-axis of the images. After reaching the desired elongation, the specimen was unloaded and SEM (Cross Beam 340 SEM, Fa. Carl Zeiss SMT) and EBSD images (Symmetry, Oxford Instruments) were recorded, before the specimen was loaded to the next defined elongation. The loading over time and the resulting elongation over time are given in Figures 1(a) and (b). The elongation steps were 0, 100, 150, 250, 500, 1000, 2000, 4000, 6000, 8000 and 14,000 μm. However, only the steps 0, 1000, 2000, 4000, 6000 and 8000 μm, which correspond to 0, 5, 10, 20, 30 and 40 pct strain, were selected for analysis, as in the steps from 0 to 1000 μm no significant changes were observed and above 8000 μm the deformation of the sample was too large for an EBSD evaluation. The step
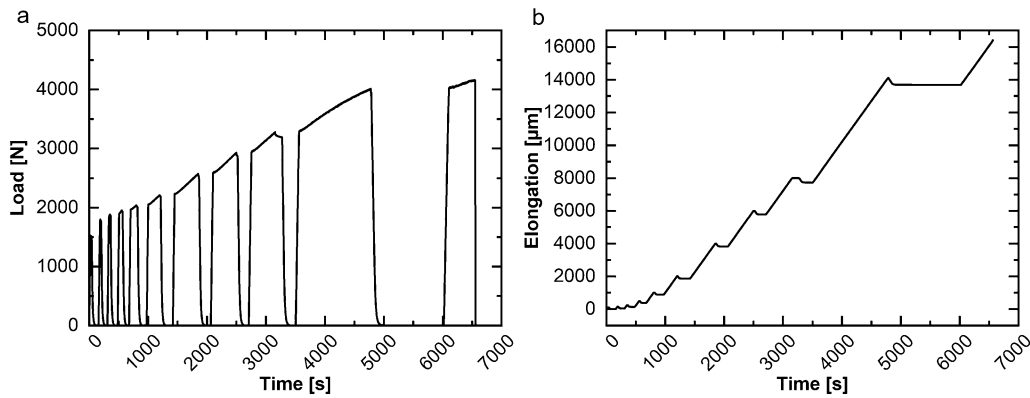
Fig. 1—Interrupted in situ tensile testing. (*a*) Load cycles and (*b*) Evolution of elongation with time.

size for the detail images was 70 nm and for the overview images it was between 0.8 and 2.2 μm (before deformation). For EBSD data analysis the Software AZtecCrystal 2.1 from Oxford Instruments was used. No clean up was carried out. The misorientation within a grain was determined by evaluating the averaged orientation difference between a kernel point and the neighboring points. This Kernel Average Misorientation (KAM) was evaluated with a kernel size of 3 × 3.

III. RESULTS

A. *Analysis of Tensile Tests*

Interrupted in situ tensile testing with a flat specimen led to a strain hardening from 360 to 830 MPa and 82 pct elongation before fracture. The resulting plot is shown in (Figure 2). However, during the in situ tensile test, the recorded elongations refer to the tensile stage movement. Subsequently, the strain values were calculated based on these elongations. The specimen thickness after electropolishing was estimated to be 1 mm
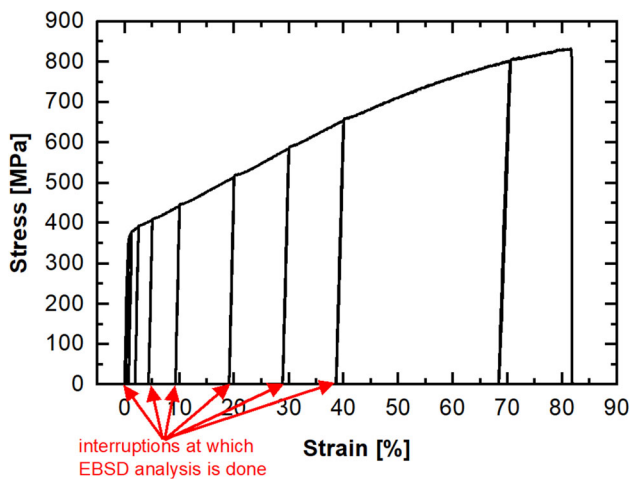

Fig. 2—Response to in situ interrupted tensile testing. The EBSD and SEM analyses were done after unloading after 5, 10, 20, 30 and 40 pct strain, as indicated by the arrows.

(see Experimental), however, this assumption leads to an uncertainty concerning the quantitative stress values which are at the ultimate tensile strength in the range of ± 200 MPa and at the yield strength in the range of ± 200 MPa.

The result of the macroscopic conventional tensile test with a round specimen but without any interruption is shown in Figures 3(a) and (b). The measured yield strength was 325 MPa. The elongation at fracture was 45 pct and the strain hardening reached 620 MPa. The difference in the results of the macroscopic conventional tensile to the interrupted tensile tests are originated from the very thin flat electropolished sample which varies in thickness used for the interrupted tests. Furthermore, the testing machine and the measurement of the elongation were different and also the interruptions might lead to relaxation and thus to different deformation behavior. Following Hwang *et al.*[40] the macroscopic twinning stress was determined by the conventional tensile tests at the point at which the strain hardening rate vs. stress curve flattens and shows the lowest strain hardening rate before it increases again, see insert in Figure 3(b). The twinning stress for the Hadfield steel was therefore located at 380 MPa at a strain of 3 pct.

B. *Twinning Analysis of Hadfield Steel After Different Applied Strains*

In Figures 4(a) through (t) an overview on the microstructurally investigated positions with SEM and EBSD and their evolution during the interrupted in situ tensile test before deformation and after 5, 10, 20, 30, 40 pct strain is given. In the upper two rows (Figures 4(a)-(h)) the overview forward scattered (FS) and secondary electron (SE) images as well as inverse pole figure images in X-direction overlaid with the band contrast (IPF-X-BC) are depicted. In the row three and four (Figures 4(i)-(t)) the detail FS and IPF-X-BC images are displayed. Two different positions were investigated by SEM and EBSD on the sample. Before deformation and up to 10 pct strain position 1 was analyzed (columns one to three of Figure 4). The position 1 is marked by yellow arrows and rectangles. The rectangles indicate the image section for the detail
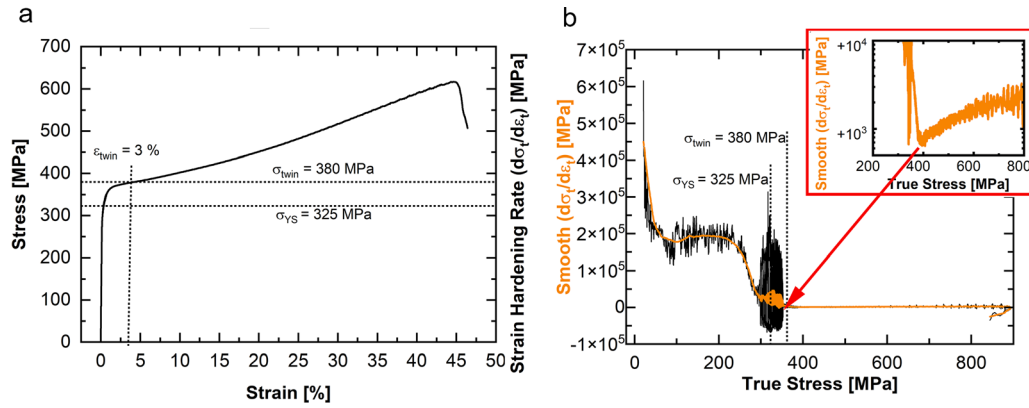
Fig. 3—Tensile test without interruption. (*a*) Engineering stress to strain curve. (*b*) Strain hardening rate vs. true stress. The yield stress was determined with 325 MPa and the twinning stress was determined with 380 MPa.
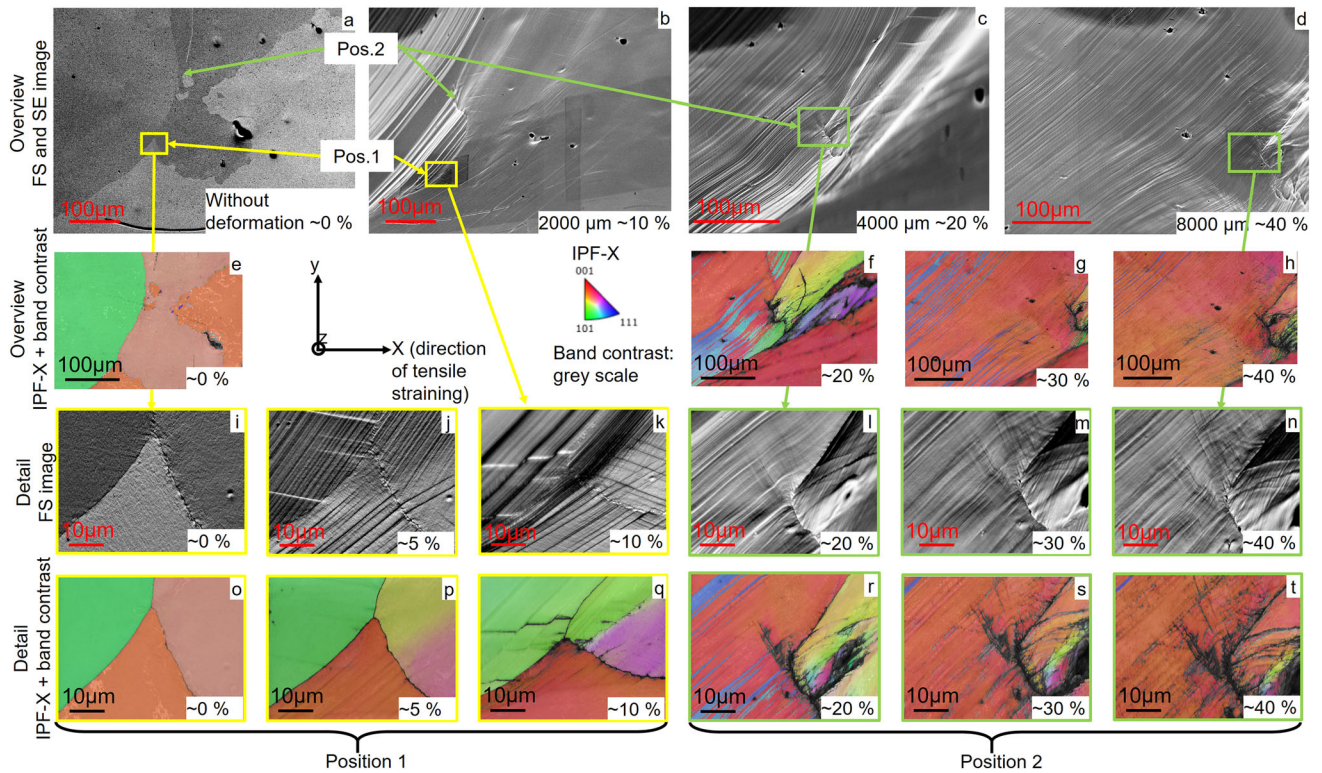

Fig. 4—Overview on selected positions for microstructure analysis on the electropolished in situ tensile test specimen with SEM and EBSD before deformation and after 5, 10, 20, 30 and 40 pct strain. Details on the sub-images are given in the text.

images of position 1. However, due to straining of the sample the surface begins to deform, so that a macroscopic relief is formed. The grain of the upper left side moved downwards along the z-direction so that the initially analyzed triple point of position 1 is no longer visible in the images with 20 pct to 40 pct elongation. Thus, for the analysis after 20 to 40 pct strain another position was selected and denoted in the following as position 2 (columns four to six of Figure 4). Position 2 is marked by green arrows and rectangles. Before deformation (Figures 4(a) and (e)) and after 10 pct (Figure 4(b)) strain both positions are visible in the overview images.

C. *Twinning Behavior Between 0 and 10 pct Strain*

Before deformation, the FS images (Figures 4(a) and (i)) exhibit no lines due to deformation and the EBSD IPF-X-BC images (Figures 4(e) and (o)) exhibits also no twins or change of orientation within the grain for both positions. After the loading/ unloading cycle to 5 pct strain, the first topographical effects in form of deformation lines are visible in the detail FS image for position 1 (Figure 4(j)). In the EBSD IPF-X-BC image (Figure 4(p)) a slight tilt over the whole grain on the upper side left but no twins were observed only by analyzing the IPF mapping. After the loading cycle to 10

pct elongation, the images show additional deformation lines and also the formation of a macroscopic relief (Figures 4(b) and (k)). In the EBSD IPF-X-BC detail image after 10 pct strain (Figure 4(q)) no change of orientation at positions of deformation lines and again no twins are observed only by analyzing the IPF mapping but the small tilt of the grain on the upper left is more pronounced compared to the image after 5 pct strain. However, evaluating EBSD mappings at 5 pct and 10 pct strain regarding pole figures in detail, indicates the presence of small twins (Figures 5 and 6). For analysis, three positions at deformations lines were selected, which are indicated by yellow rectangles in Figures 5(a), 6(a), and (d). The magnified sections of these rectangles after 5 pct and 10 pct strain are shown by the IPF-X-BC images in Figures 5(b), 6(b), and (e). At these positions, single pixels (indicated by arrows) with 60 deg rotation of the {111}-planes are present, as visible by the pole figure analysis in Figures 5(c), 6(c) and (f). These single pixels are spread over the whole area of the deformation lines and show the same orientation. It is also pointed out that in the magnified 10 pct strain IPF-X-BC image (Figure 6(b)) two different twin systems are present. One in the horizontal deformation line (dark green pixels) and another one in the diagonal lines (orange pixels). Such single pixels with a Σ3 coincidence were found at several positions after 5 and 10 pct strain.

D. Twinning Behavior Between 20 and 40 pct Strain

In the SE overview images of Figures 4(c) and (d) only position 2 is visible at interruption after 20 pct and 40 pct strain, position 1 is hidden by the sample itself due to surface deformation. However, a lot of deformation lines are visible after 20 pct to 40 pct strain in the SE and FS images of position 2 in Figures 4(c), (d) and (l)-(n). The overview and the detail IPF-X-BC pictures of position 2 after 20 pct to 40 pct in Figures 4(f) through (h) and (r)-(t) reveal that at least some of these lines are twins. Many twins have formed after the loading/unloading cycle to 20 pct strain and
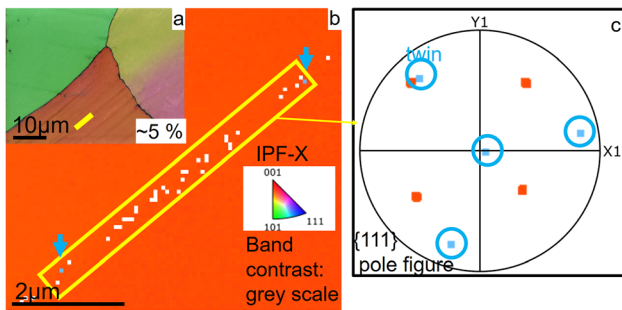

Fig. 5—Pole figure analysis of the selected region after 5 pct strain. (a) IPF-X-BC image after 5 pct strain with a marked position (yellow rectangle) at a deformation line. (b) The marked region is magnified. The IPF-X image shows blue pixels which have a different orientation with respect to the matrix. In (c) it is illustrated by the pole figure analysis of the marked region that the blue pixels within the deformation line exhibit a Σ3 coincidence and correspond to twins that are rotated by 60 deg with respect to the {111}-plane (Color figure online).

the twinned regions are relatively thick (7 μm), whereas the thickness of the twinned regions and amount of the twins are reduced in the images after the loading/unloading cycle to 30 pct strain and nearly all twins except a few thin ones vanish due to the cycle to 40 pct strain. The thickness of the twinned regions was approx. 4 μm after 30 pct and 2 μm after 40 pct strain. The presence of twins was determined by the pole figure analysis shown in Figure 7. After 20 pct strain the pole figure analysis shows only the matrix and Σ3 twins with 60 deg rotation of the {111}-plane. However, after the loading cycle to 30 pct strain not only Σ3 twins and the matrix are visible in the {111} pole figure, but further orientations. It was determined that these orientations are located near the twins and might be a result of the large deformation already present at this condition. The interruption after 40 pct strain exhibits also Σ3 twins and various different other orientations owing to the deformation.

E. Characterization of Misorientation

The misorientation within the grains and twins, caused in most cases by dislocations, can be determined by the Kernel Average Misorientation (KAM). The KAM is used in this work to identify the influence of deformation, twinning and detwinning. In Figure 8 detail and overview EBSD IPF-X-BC and KAM images of positions 1 and 2 are displayed. Before deformation (position 1, overview and detail image (Figures 8(a), (g), (m) and (q)) the KAM is low (< 0.5 pct) and no deformation lines are visible. After straining to 5 pct and 10 pct elongation the first deformation lines with a higher KAM evolve (Figures 8(b), (c), (h) and (f)). At the position of these lines, twins might have formed, as also some higher KAM (> 0.5 pct) values are at the position of the small twins determined in Figure 6. After 20 pct elongation (Figures 8(d), (j), (n) and (r)) twins have formed at the position 2. These twins show a higher KAM compared to the untwinned regions. In the untwinned regions, the KAM is low. However, there are some positions of low KAM within some twins (indicated by the black arrows). After the loading/unloading cycle at 30 pct and 40 pct strain (Figures 8(e), (f), (k), (l), (o), (p) through (t)) most of the twins have vanished and in some cases (white arrows) high KAM values persist at the former positions of the twins. Generally, the KAM increases with increasing elongation over the whole image.

IV. DISCUSSION

A. Twinning

In the present work, an interrupted in situ tensile test was carried out in SEM coupled with EBSD analysis and for comparison a conventional tensile test without interruption was conducted. The findings of the conventional tensile test showed that according to the analysis of the macroscopic twinning stress,[40] the first twins form at 380 MPa which is reached after about 3
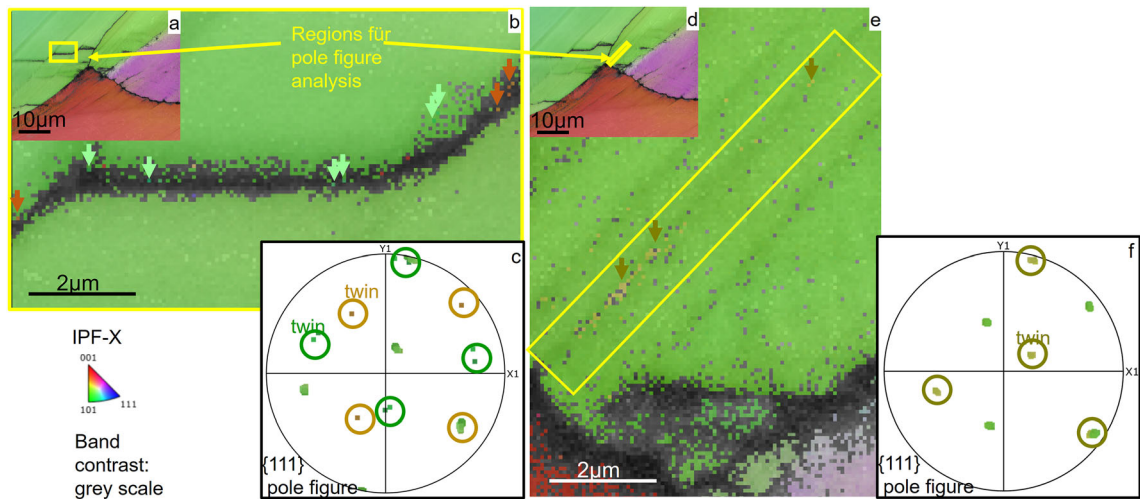
Fig. 6—Pole figure analyses of selected regions after 10 pct strain. The magnified IPF-X-BC image in (*b*) of the marked region in (*a*) shows a deformation line. Within this line different orientations are visible, *i.e.* dark green pixels horizontally and orange pixels diagonally, marked by arrows. The pole figure analysis (*c*) for the marked region determines two different oriented twins. The twins exhibit a rotation of 60 deg to the matrix and are thus Σ3 twins. The magnified IPF-X-BC image in (*e*) of the marked region in (*d*) shows a deformation line. Within this line, a different orientation compared to the matrix is visible, *i.e.* a band of yellow pixels marked by arrows along the deformation line. The pole figure analysis (*f*) for the marked region determines the presence of a twin in the deformation line. The twin exhibits a rotation of 60 deg and is thus a Σ3 twin (Color figure online).
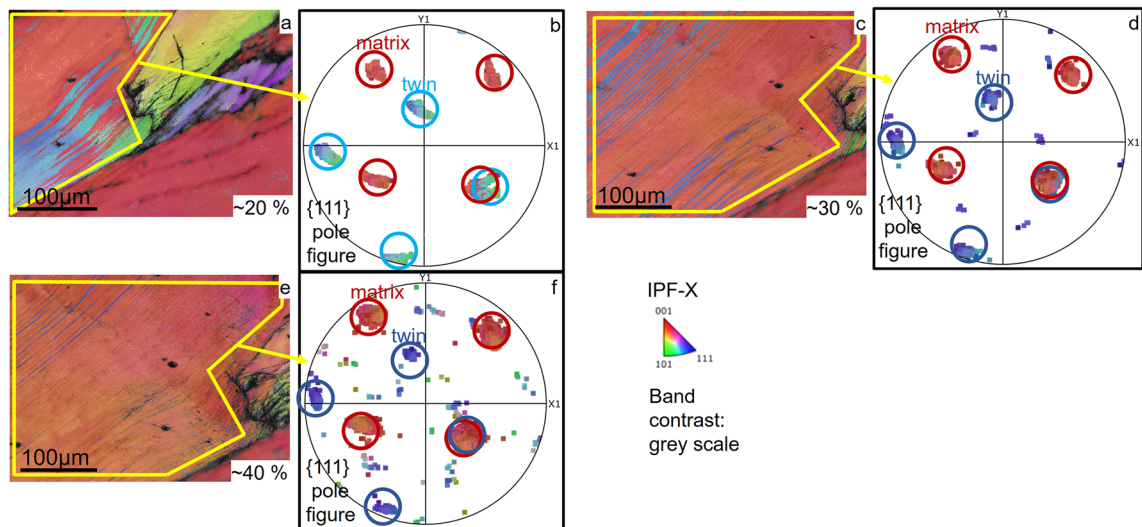

Fig. 7—Pole figures of the overview images after 20 to 40 pct strain. In (*a*) the position within the twinned grain after 20 pct strain is marked for pole figure analysis of the twin in (*b*). In (*c*) the position within the twinned grain after 30 pct strain is marked for pole figure analysis of the twin in (*d*). In (*e*) the position within the twinned grain after 40 pct strain is marked for pole figure analysis of the twin in (*f*). The positions were selected within the grain to avoid effects from the grain boundaries. The {111}-pole figure analysis showed Σ3 twins.

pct strain. The results of the interrupted tensile test in SEM suggest that twins have formed after 5 to 10 pct strain. These twins were determined in form of single pixels at deformation lines with a Σ3 coincidence. Especially, after 5 pct strain only very few pixels with twinning orientation at deformation lines are present (Figure 5). Thus, it was checked if these pixels belong to pseudo-symmetries (according to[44]), resulting that pseudo-symmetries can be excluded for the pixels after the loading and unloading cycles to 5 and 10 pct strain (Figures 5 and 6). Previous works[14,28,29] determined that deformation twins form as a bundle of twins. The

first deformation twin that forms exhibits a thickness of about 10 to 40 nm. Upon further straining further twins form near the first one with a similar thickness extending the twin to a thicker twin bundle. In this work, the thickness of analyzable twin bundles is estimated to be larger than 70 to 100 nm, as the step size for EBSD measurements was 70 nm and the accompanying image resolution would be at or above 70 nm. Thus, due to the limited EBSD image resolution and the characterization of only a few grains an exact determination of the start of twinning is not possible as smaller twins or twins formed at lower strain amplitudes in differently
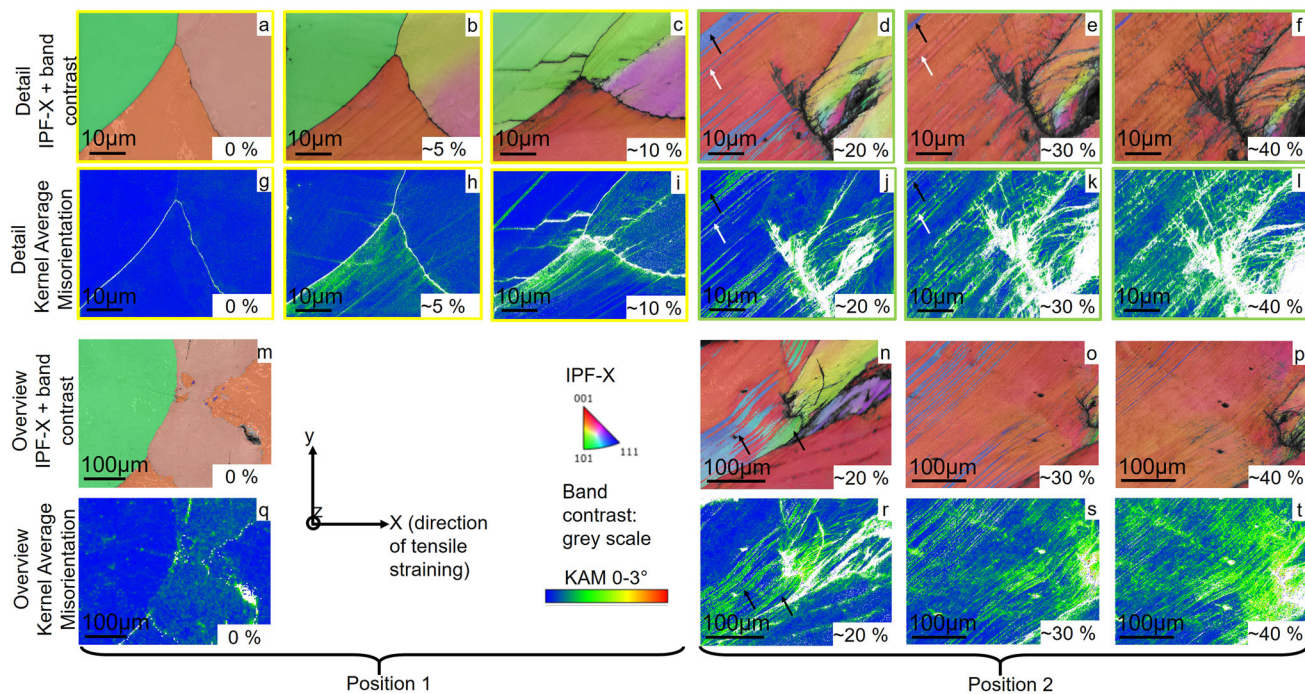
Fig. 8—Comparison of Kernel Average Misorientation (KAM) with IPF-X-BC images. (*a, g, m, q*) IPF-X-BC and KAM images before deformation. A low KAM is present in the detail and overview images of position 1 and 2. (*b-c*) and (*h-i*) IPF-X-BC and KAM images after 5 and 10 pct strain. The KAM increases at the position of deformation lines (position 1). (*d-f*), (*j-l*), (*n-p*) and (*r-t*) IPF-X-BC and KAM images after 20 to 40 pct strain. The detail and overview images of position 2 show higher KAM values at the position of the twins. But also regions of low KAM at the positions of twins are present, as indicated by the black arrows. White arrows indicate positions where twins have vanished but high KAM values remained (Color figure online).

orientated grains might be undetected by the used experimental setup in this work. However, a contribution to the knowledge on the early stages of twin formation in TWIP steel can be given, confirming the results of works.[41,43,45] Twin formation is described *via* the formation of stacking faults by the dissociation of a perfect < 110 > dislocation on an {111} plane into two < 112 > Shockey partial dislocations. Adjacent stacking faults on {111} planes form twin embryos with a critical width.[45] Others describe that twins are formed after the Shockley partial interacts with a Lomer-Cotrell lock.[41,43]

However, Barbier *et al.*[29] found twin bundles after 2 pct strain in a Fe-22Mn-0.6C steel with TEM experiments, whereas EBSD measurements reveal the first twins bundles between 10 to 20 pct strain. This is in relatively good coincidence with this work, as the analysis of the macroscopic twinning stress according to Hwang[40] showed that twins formed at 380 MPa which is reached after about 3 pct strain and the first traces of twins were found with EBSD after 5 to 10 pct strain at deformation lines. Thus, it can be deduced that twins may even be present at low strain values (around 3 pct), but the image resolution of EBSD is not sufficient for displaying the small twin bundles. By increasing the strain to 5 pct the twin bundles become thicker and can be analyzed by EBSD. It is to mention that the deformation lines, which may indicate twins have formed already after about 0.75 pct strain, as depicted in Figure 9.

The EBSD analysis done during the interruption of the tensile test after the loading/unloading cycle to 20 pct strain indicates that a massive twin formation has already occurred. The thickness of twin bundles increased to 7 μm (Figures 4(c), (f), (l) and (r)). Within the formed twin bundles the KAM shows higher values compared to the untwinned matrix (see Figure 8). Higher KAM values can be linked to a higher dislocation density. Wu and Bei[42] also analyzed that in the twinned regions, especially at the interfaces between twin and untwinned matrix a lot of dislocations accumulate as formation of twins is accompanied by dislocation generation. Furthermore, Idrissi *et al.*[41] revealed that twins are formed according to the pole mechanism with deviation initially proposed by Cohen and Weertman[43]: A perfect dislocation on the primary plane dissociates into a sessile Frank partial and a glissile Shockley partial dislocation after passing a Lomer-Cotrell barrier. The Shockley partial glides away from the sessile dislocation on the conjugate twinning plane and by this the starting point for the formation of a twin is set. Irdissi *et al.*[41] determined a lot of sessile dislocations in twins, which leads to a strengthening effect and also to an increase of KAM within twin bundles as found in this work.

B. Detwinning

After the loading/unloading cycle to 30 pct strain the thickness of twin bundles decreases to 4 μm and the
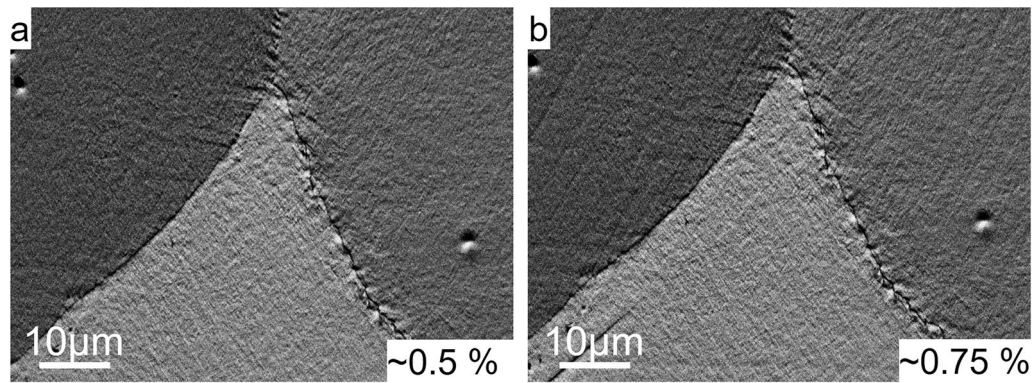
Fig. 9—The first deformation lines form after 0.75 pct strain. In (a) the FS detail image of position 1 after 0.5 pct strain is displayed. No deformation lines are visible. In (b) the image after 0.75 pct strain shows a deformation line.

amount of twin bundles is reduced (Figures 4(g), (m) and (s)). A further cycle to 40 pct strain results in further reduction of deformation twins and the thickness of twin bundles was reduced to 2 μm (Figures 4(d), (h), (n) and (t)). The reduction of deformation twins upon further loading/unloading cycles is linked to detwinning. On the nm scale detwinning can be explained by dislocation reaction with twin interfaces—e.g. a partial dislocation which reacts with the twin boundary and by that reaction with dislocations the twin thickness is reduced atom layer by atom layer.[34,46] Detwinning was also reported in former studies after load reversal.[14,36,37] However, in the present work it is the first time that detwinning is observed for Hadfield Steel after unloading by EBSD. Detwinning is explained by McCormack et al.[14] by backstresses introduced during twin formation, which enable detwinning when reaching the critical detwinning stress during load reversal. In this work no load reversal was applied but straining to 30 pct elongation leads to plastic deformation. Some grain orientation might be strained even more than others which is dependent on the orientation dependent elastic and plastic properties.[47] It is assumed that during unloading, some of the intensively plastically deformed regions in tension might be under compressive stresses, which are high enough to promote detwinning. Detwinning upon unloading was also shown by Hu et al.[48] by phase field modeling. Furthermore, as it is indicated that detwinning occurs during unloading owing to internal local stress fields, it is suggested that detwinning is a result of the frequency and setup of loading/unloading cycles. Additionally, as twins have vanished after 40 pct strain detwinning gets more favorable than twinning during cyclic loading. Thus, also plastic deformation by dislocations is favored during cyclic loading compared to twinning during static loading.

It was also found that the KAM generally increases with increasing strain, even in the regions, where no twinning took place (see Figure 8). This is due to the raise of dislocation density due to straining. At the twinned regions a high KAM is observable. Detwinning leads to reduction of the KAM but some detwinned regions with higher KAM values also exist (white arrows in Figures 8(d), (e), (j) and (k)). It is described

by Szczerba et al.[36,37] that only one detwinning system out of three possible is reversible (transforms to initial matrix orientation with initial dislocation structure), the other two lead to pseudo reverse detwinning and the introduction of shear strains and thus, to a raise of dislocations, which increase the KAM (transformation to initial orientation with increased dislocation density). Therefore, it is possible that at some positions the higher KAM after detwinning persists where pseudo reverse detwinning takes place, where at other positions where reversible detwinning occurs the KAM decreases as twins have vanished. However, also low KAM values in twinned regions were found after the loading/unloading cycle to 20 pct strain (black arrows in Figures 8(d), (e), (j), (k), (n) and (r)). In these twinned regions with low KAM larger twins with up to 5 μm (measured from figure) might be located. Maybe one should see this area as single twin and not as bundle. As it is a single twin no interfaces are present as in case of the bundle and therefore also a lower amount of dislocations would be present resulting in low KAM values. It is interesting to see that the twinned region with low KAM from the detail image of position 2 (Figures 8(d) through (f)) does not untwin even after the loading/unloading cycle to 30 pct and 40 pct strain. According to McCormack and Ni et al.[14,34] detwinning mechanism is based on a dislocation interaction which removes the twinned area sequentially atom layer by atom layer. Consequently, a thick twin needs more strain cycles than the smaller ones to untwin.

V. CONCLUSION

In the present work, the behavior of the Hadfield steel during interrupted tensile testing coupled with EBSD and SEM analysis was characterized. The results show:

- The analysis of the macroscopic twinning stress showed, that twinning starts at about 3 pct strain but single twins are too thin for EBSD image resolution. After 5 to 10 pct strain, the first traces of small twin bundles in the size of the EBSD image resolution (above 70 to 100 nm) were found by the detection of single pixels in twinning orientation.

- Massive twinning takes place due to straining to 20 pct. Twin bundles have a thickness of 7 μm and a high KAM which is a result of twinning as it is accompanied by the formation of dislocations.
- Further loading/unloading cycles to 30 pct and to 40 pct elongation lead to partial detwinning upon unloading. Both detwinning and twinning take place by distinct dislocation reactions which transfer the orientation layer by layer. Thus, for detwinning the thickness of the twin bundles decreases with every loading cycle. The thickness is 4 μm after the cycle to 30 pct and to 2 μm after the cycle to 40 pct strain.
- In this work also twined regions with low KAM were found. It is claimed that these regions consist of larger single twins and not of bundles. At the positions with low KAM and thus larger twins, the detwinning takes place more slowly, supporting the layer by layer detwinning mechanism.
- Due to detwinning the KAM is not completely reduced. As also previous works stated, detwinning in some cases is not completely reversible, thus dislocations may persist after detwinning.
- In contrast to most of the other studies, this work shows detwinning during loading/unloading cycles and not during reverse loading. It is suggested that detwinning takes place during unloading due to compressive stresses, which are a result of plastic deformation of some favorable orientated grains for deformation during loading.
- Due to the cyclic character of the loading unloading sequences in this work, it is claimed that detwinning plays a greater role in the deformation behavior during cyclic loading.

CONFLICT OF INTEREST

On behalf of all authors, the corresponding author states that there is no conflict of interest.

REFERENCES

1. G. Tweedale: *Notes Rec. R. Soc. Lond.*, 1985, vol. 40, pp. 63–74.
2. Y.N. Dastur and W.C. Leslie: *Metall. Trans. A*, 1981, vol. 12A, pp. 749–59.
3. L. Chen, Y. Zhao, and X. Qin: *Acta Metall. Sin. (Eng. Lett.)*, 2013, vol. 26, pp. 1–5.
4. M. Koyama, T. Sawaguchi, T. Lee, C.S. Lee, and K. Tsuzaki: *Mater. Sci. Eng. A*, 2011, vol. 528, pp. 7310–16.
5. C. Scott, S. Allain, M.M. Faral, and N. Guelton: *Revue de Métallurgie*, 2006, vol. 103, pp. 293–302.
6. K.T. Park, K.G. Jin, S.H. Han, S.W. Hwang, K. Choi, and C.S. Lee: *Mater. Sci. Eng. A*, 2010, vol. 527, pp. 3651–61.
7. R. Harzallah, A. Mouftiez, E. Felder, S. Hariri, and J.-P. Maujean: *Wear*, 2010, vol. 269, pp. 647–54.
8. P.H. Adler, G.B. Olson, and W.S. Owen: *Metall. Mater. Trans. A*, 1986, vol. 17A, pp. 1725–37.
9. V. Läpple, B. Drube, G. Wittke, and C. Kammer: *Werkstofftechnik Maschinenbau*, 4th ed. Europa Lehrmittel, Haan Gruiten, 2013.
10. A.A. Gulyaev, Y.D. Tyapkin, V.A. Golikov, and V.S. Zharinova: *Met. Sci. Heat Treat.*, 1985, vol. 27, pp. 411–15.
11. S.B. Sant and R.W. Smith: *J. Mater. Sci.*, 1987, vol. 22, pp. 1808–14.
12. I. Karaman, H. Sehitoglu, Y.I. Chumlyakov, H.J. Maier, and I.V. Kireeva: *Scr. Mater.*, 2001, vol. 44, pp. 337–43.
13. W.D. Callister and D.G. Rethwisch: *Materials Science and Engineering*, 8th ed. Wiley, Hoboken, 2011.
14. S.J. McCormack, W. Wen, E.V. Pereloma, C.N. Tomé, A.A. Gazder, and A.A. Saleh: *Acta Mater.*, 2018, vol. 156, pp. 172–82.
15. ASTM International: *ASTM A128 / A128M-93(2012), Standard Specification for Steel Castings, Austenitic Manganese*, 2012.
16. A. Saeed-Akbari, L. Mosecker, A. Schwedt, and W. Bleck: *Metall. Mater. Trans. A*, 2012, vol. 43A, pp. 1688–704.
17. J. Kang and F.C. Zhang: *Mater. Sci. Eng. A*, 2012, vol. 558, pp. 623–31.
18. O. Bouaziz, H. Zurob, B. Chehab, J.D. Embury, S. Allain, and M. Huang: *Mater. Sci. Technol.*, 2011, vol. 27, pp. 707–09.
19. E. Bayraktar, F.A. Khalid, and C. Levaillant: *J. Mater. Process. Technol.*, 2004, vol. 147, pp. 145–54.
20. J. Kang, F.C. Zhang, X.Y. Long, and B. Lv: *Mater. Sci. Eng. A*, 2014, vol. 591, pp. 59–68.
21. E.G. Astafurova, M.S. Tukeeva, G.G. Maier, E.V. Melnikov, and H.J. Maier: *Mater. Sci. Eng. A*, 2014, vol. 604, pp. 166–75.
22. V.G. Gavriljuk, O. Razumov, Yu. Petrov, I. Surzhenko, and H. Berns: *Steel Res. Int.*, 2007, vol. 78, pp. 720–23.
23. G. Gottstein: *Physikalische Grundlagen der Materialkunde*, 3rd ed. Springer, Berlin, Heidelberg, 2007.
24. J.W. Christian and S. Mahajan: *Prog. Mater. Sci.*, 1995, vol. 39, pp. 1–57.
25. M.S. Szczerba, T. Bajor, and T. Tokarski: *Philos. Mag.*, 2004, vol. 84, pp. 481–502.
26. B.C. De Cooman, Y. Estrin, and S.K. Kim: *Acta Mater.*, 2018, vol. 142, pp. 283–362.
27. B.C. De Cooman, O. Kwon, and K.-G. Chin: *Mater. Sci. Technol.*, 2012, vol. 28, pp. 513–27.
28. A. Albou, M. Galceran, K. Renard, S. Godet, and P.J. Jacques: *Scr. Mater.*, 2013, vol. 68, pp. 400–03.
29. D. Barbier, N. Gex, N. Bozzolo, S. Allain, and M. Humbert: *J. Microsc.*, 2009, vol. 235, pp. 67–78.
30. Q. Wang, B. Jiang, J. Zhao, D. Zhang, G. Huang, and F. Pan: *Mater. Sci. Eng. A*, 2020, vol. 798, pp. 2–10.
31. L. Song, B. Wu, L. Zhang, X. Du, Y. Wang, C. Esling, and M.-J. Philippe: *Mater. Charact.*, 2019, vol. 148, pp. 63–70.
32. A. Vinogradov, E. Vasilev, M. Linderov, and D. Merson: *Mater. Sci. Eng. A*, 2016, vol. 676, pp. 351–60.
33. Y.B. Wang and M.L. Sui: *Appl. Phys. Lett.*, 2009, vol. 94, p. 021909. https://doi.org/10.1063/1.3072801.
34. S. Ni, Y.B. Wang, X.Z. Liao, H.Q. Li, R.B. Figueiredo, S.P. Ringer, T.G. Langdon, and Y.T. Zhu: *Phys. Rev. B*, 2011, https://doi.org/10.1103/PhysRevB.84.235401.
35. Y. Cao, Y.B. Wang, Z.B. Chen, X.Z. Liao, M. Kawasaki, S.P. Ringer, T.G. Langdon, and Y.T. Zhu: *Mater. Sci. Eng. A*, 2013, vol. 578, pp. 110–14.
36. M.J. Szczerba, S. Kopacz, and M.S. Szczerba: *Acta Mater.*, 2016, vol. 102, pp. 162–68.
37. M.J. Szczerba, S. Kopacz, and M.S. Szczerba: *Acta Mater.*, 2016, vol. 104, pp. 52–61.
38. C. D'Hondt, V. Doquet, and J.P. Couzini: *Mater. Sci. Eng. A*, 2021, vol. 814, p. 141250.

39. R. Mohammadzadeh: *Mater. Sci. Eng. A*, 2020, vol. 782, p. 139251. https://doi.org/10.1016/j.msea.2020.139251.
40. J.-K. Hwang: *Mater. Sci. Eng. A*, 2020, vol. 772, p. 138709. https://doi.org/10.1016/j.msea.2019.138709.
41. H. Idrissi, K. Renard, L. Ryelandt, D. Schryvers, and P.J. Jacques: *Acta Mater.*, 2010, vol. 58, pp. 2464–76.
42. Z. Wu and H. Bei: *Mater. Sci. Eng. A*, 2015, vol. 640, pp. 217–24.
43. J.B. Cohen and J. Weertman: *Acta Metall.*, 1963, vol. 11, pp. 996–98.
44. T. Karthikeyan, M.K. Dash, S. Saroja, and M. Vijayalakshmi: *J. Microsc.*, 2013, vol. 249, pp. 26–33. https://doi.org/10.1111/j.1365-2818.2012.03676.x.
45. E.I. Galindo-Nava and P.E. Rivera-Díaz-del-Castillo: *Acta Mater.*, 2017, vol. 128, pp. 120–34.
46. X. An, S. Ni, M. Song, and X. Liao: *Adv. Eng. Mater.*, 2020, vol. 22, p. 1900479. https://doi.org/10.1002/adem.201900479.
47. I. Karaman, H. Sehitoglu, K. Gall, Y.I. Chumlyakov, and H.J. Maier: *Acta Mater.*, 2000, vol. 48, pp. 1345–59.
48. S.Y. Hu, C.H. Henager Jr., and L.Q. Chen: *Acta Mater.*, 2010, vol. 58, pp. 6554–64.